Title: **Mechanism of Phosphate Release from Actin Filaments**

Yihang Wang[a], Vilmos Zsolnay,[b] Thomas D. Pollard,[c,d,e,*] and Gregory A. Voth[a,1]

[a]Department of Chemistry, Chicago Center for Theoretical Chemistry, Institute for Biophysical Dynamics and James Frank Institute, University of Chicago, Chicago, IL
[b]Graduate Program in Biophysical Sciences, University of Chicago, Chicago, IL
[c]Department of Molecular Cellular and Developmental Biology, Yale University, New Haven, CT
[d]Department of Molecular Biophysics and Biochemistry, Yale University, New Haven, CT
[e]Department of Cell Biology, Yale University, New Haven, CT
*Current address: Department of Cell and Molecular Biology, University of California, Berkeley

[1]Corresponding authors: **Email:** gavoth@uchicago.edu; thomas.pollard@yale.edu

Keywords
Actin filament, ATP, phosphate, molecular dynamics, machine learning

Author Contributions
Y.W., V.Z. and G.A.V. designed research; V.Z. and Y.W. performed research; Y.W., V.Z., G.A.V., and T.D.P. analyzed data; Y.W., V.Z. , G.A.V., and T.D.P. wrote the paper.

Abstract
After ATP-actin monomers assemble filaments, the γ-phosphate is hydrolyzed from ATP within seconds and dissociates from the filament over several minutes. We used all-atom 2-dimensional well-tempered metadynamics computer simulations to sample the release of phosphate from filaments with unbiased molecular dynamics simulations to study residues that gate release. Dissociation of phosphate from Mg^{2+} is rate limiting and associated with an energy barrier of 20 kcal/mol, consistent with experimental rates of phosphate release. Phosphate then diffuses in an internal cavity toward a gate formed by R177 recognized in prior computational studies and cryo-EM structures. The gate is closed when R177 hydrogen bonds with N111 and is open when R177 forms a salt bridge with D179. Most of the time interactions of R177 with other residues

occludes the phosphate release pathway. Machine learning analysis reveals that the occluding interactions fluctuate rapidly. These occluded states have not yet been documented in cryo-EM reconstructions. (150 words)

Significance Statement

The protein actin assembles into filaments that participate in muscle contraction and other cellular movements. An ATP bound to the actin monomer is hydrolyzed rapidly during filament assembly, but the γ-phosphate dissociates slowly from the filament. We used molecular dynamics simulations to characterize the slow release process. Separation of phosphate from Mg^{2+} in the active site is rate limiting owing to a large free energy barrier 20 kcal/mol. Release of phosphate from the protein requires opening a gate in the actin molecule formed by interaction of the sidechains of arginine 177 and asparagine 111. Surprisingly, the simulations revealed other interactions of the sidechain of arginine 177 that occlude the release pathway most of the time but have not been observed in cryo-EM structures. (124 words)

Introduction

Living cells recycle actin molecules countless times by assembly and disassembly of filaments that they use for cellular movements and physical support of the cell and its plasma membrane. During each cycle of assembly, actin molecules with bound Mg-ATP from the cytoplasm (1) incorporate at one of the two ends of a filament (largely the fast-growing "barbed" end) (2) and undergo a conformational change that flattens the twisted actin monomer (3-5). Flattening repositions residues in the active site and activates the ATPase activity of the subunit about 42,000-fold (6, 7) with a half time of 2 s, producing ADP and an $H_2PO_4^-$ ion, henceforth called phosphate (P_i), to form an intermediate, Mg-ADP-P_i-actin. The reaction occurs by either a dissociative pathway, where the ß-γ-phosphate bond breaks prior to the addition of lytic water, or a concerted mechanism, where the γ-phosphate bond breaks concurrently with the addition of lytic water(6, 8-15). Although hydrolysis releases free energy, the structures of ATP- and Mg-ADP-P_i-actin subunits are identical (4). The free γ-phosphate escapes into solution very slowly with a half time of 6 min (16). Filaments with ADP-actin subunits differ those with ATP or ADP-P_i-actin subunits in stiffness,(17-21) affinities for regulatory proteins such as cofilin,(22, 23) and the response to stresses (24, 25).

In spite of ever higher resolution structures of actin filaments, now extending to < 2.5 Å resolution (26, 27), the mechanism of slow phosphate release is still in question. Wriggers and Schulten (28) concluded from steered molecular dynamics (SMD) simulations that phosphate is released from monomeric actin by a pathway from the active site to a "backdoor" near methylhistidine HIC73 in subdomain 1 (SD1). They limited their analysis to an assumed a predefined pathway and applied an external force to pull phosphate along to exit actin. Along this path the phosphate interacts with several residues including S14, G74, G158, H161 and V159. The rate limiting step in their simulations was dissociation of phosphate from the divalent cation in the active site, assumed to be Ca^{2+} rather than the physiological Mg^{2+}. Cryo-EM structures of actin filaments with bound AMPPNP (an ATP analog)-, ADP-P_i-, and ADP-actin filaments nucleotides suggested a possible exit gate formed by R177, N111, and HIC73, which was closed in the ADP-P_i-actin structure and open in the ADP-actin structure. A possible mechanism is that as phosphate dissociates from the Mg^{2+} ion, a hydrogen bond (H-bond) between S14 and G74 breaks making SD2 more flexible and favoring rotation of the side chain of HIC-73 to open the exit gate. On the other hand, the N111-R177 exit gate was closed in higher resolution cryo-EM structures of ADP-P_i-, and ADP-actin filaments (26, 27).

We use well-tempered metadynamics (WT-MetaD) (29-32) biased free energy sampling and unbiased molecular dynamics (MD) simulations to investigate the release of P_i from Mg-ADP-P_i-actin filaments. We find a 20.5 kcal/mol free energy barrier associated with breaking the bond between Mg^{2+} and the $H_2PO_4^-$ ion, which is in good agreement with the experimental time scale for P_i release according to a simple transition state theory estimate. Once free from Mg^{2+}, P_i diffuses through an internal cavity to a gate formed by the side chain of R177 in subdomain 3. Three different hydrogen bonding interactions of R177 explain the three different states of channel connected to the exterior. Formation of a hydrogen-bond between the side chains of R177 and N111 in subdomain 1 closes the gate. Alternately, the sidechain of R177 can bend toward the interior of the protein and form hydrogen bonds with H161 and P109, which also occludes the channel. Formation of a hydrogen bond with H73 and a salt bridge with D179 opens the gate on the channel. During unbiased MD simulations, actin spends most of the time in the occluded state but also visits the closed and open states. The residence time in the occluded and closed states slows phosphate release, but it is not the rate-limiting step in our simulations.

Results

Preparation of a pentameric ADP-P_i actin filament for MD simulations. We used both well-tempered metadynamics (WT-MetaD) and unbiased MD simulations to investigate the release of P_i from a subunit in a short, ADP-P_i-actin filament with five subunits named from the barbed end A0-A4 (Fig. 1A). We focused on the middle subunit A_2 within the accessible time in all the simulations. We prepared these pentamers as follows:

Starting a 13-subunit section of the Chou (4) cryo-EM structure of the ADP-P_i-actin filament (PDB 6DJN), Zsolnay et al. carried out computational solvation and equilibration (33), which produced a filament with altered subunits on the ends and a core of conventional subunits in the occluded state (defined below) with helical parameters similar to the cryo-EM structure.

We took five conventional subunits from the core of the 13-mer filament and further equilibrated the system with energy minimization and a 10 ns simulation with a constant number of particles, pressure, temperature (NPT) **(Fig 1A)**. This resulted in flattening of the terminal subunits at the barbed end and partially twisting the of the terminal subunits at the pointed end. The central subunit A2 was flattened with an occluded phosphate release pathway, described in detail below. We used this structure as the initial structure in the unconstrained MD simulations.

The altered conformations of the subunits flanking subunit A2 may influence the release of phosphate, so we carried out four additional constrained simulations with restraints to maintain the flattened state of the terminal subunits flanking the central subunit. The initial structure for the constrained simulations was prepared by using steered MD to drive all the subunits into the flattened state (as detailed in the Methods section, with subsequent WT-MetaD results given in the **Supplementary Materials**).

Well Tempered-MetaD simulations. During WT-MetaD simulations, the dihedral angles of all five subunits were more stable in restrained pentamer, with the central subunit A2 remaining flattened like a subunit in the core of an actin filament **(Fig. 1C)**. In four independent simulations of unrestrained and four simulations of restrained filaments, phosphate used similar pathways to move from the active site next to the ß-phosphate of ADP out of the protein next to R177, commonly called the "backdoor" pathway **(Fig. 1B)**. Furthermore, the potentials of mean force (PMFs, i.e., free energy curves) as a function of the distance between P_i and the Mg^{2+} ion were similar in the restrained and unrestrained filaments **(Fig. 1D)**. This results section therefore

focuses on simulations with unrestrained subunits but also notes similar results of simulations with retrained subunits.

The potential of mean force as phosphate is released by the "backdoor" pathway. We calculated the potential of mean force (PMF) as a function of the distance between P_i and the Mg^{2+} ion in the active site by averaging the free energy profiles of 6 independent unbinding trajectories for both the unrestrained and restrained filaments (**Fig. 1C**). The error bars in **Fig. 1 (d)** are standard errors representing the uncertainty in the PMF measurements. The small variability indicates consistency between different simulation trials, whose energy profiles are separately shown in **Supplementary Fig. S1**. The small variance between individual release trajectories and PMF also suggests that the P_i release pathway is stable. Moreover, the gentle biasing potential that we added to the system did not introduce any artifact or spurious mechanism in the simulations.

The plot in **Fig. 1D** reveals two energy barriers in the release pathway: a high barrier of ~20.5 kcal/mol close to the bound state, and another of ~5.0 kcal/mol near the unbound state. Furthermore, the PMF profile is quite similar in the simulations with restrained subunits. The difference between the PMFs from unrestrained and restrained systems is within the simulation error. Based on the positions of these energy barriers in the PMF, phosphate proceeds in three distinct stages.

Stage 1, breaking the coordination between P_i and Mg^{2+}. The first step of the release process involves the loss of coordination between phosphate and the Mg^{2+} ion, which is associated with the energy barrier located close in distance from the bound state in **Fig. 1D**. The deep energy basin at the bound state indicates strong interaction between P_i and Mg^{2+}. In addition to the coordination between P_i and Mg^{2+}, our simulations revealed stabilizing interactions between P_i in the nucleotide-binding site and the protein. P_i forms hydrogen bonds with S14 and Q137 in the initial equilibrium structure (**Fig. 2D**). During the simulations, Q137 adopted a new rotameric state (**Fig 2E**) to form hydrogen bonds with the side chain of H136 reoriented away from the P_i. The distance between P_i and Mg^{2+} increased only after disruption of the interaction between Q137 and P_i (**Supplementary Fig. S2 and Supplementary Video 1)**.

The coordination between water molecules and P_i changed in both unbiased and WT-MetaD simulations. The number of waters coordinated with Mg^{2+} was estimated using a

continuous switch function with a 3 Å cutoff (see **Supplementary Materials** for more details). On the time scale of the unbiased MD simulations, the coordination number fluctuates in a relatively wide range (2.3~4.2) (**Supplementary Fig. S3**). **Figs. 2B** and 2**C** illustrate the cases in simulations where Mg^{2+} coordinates with three or four water molecules. **Fig. 2A** compares the PMF of the P_i-Mg^{2+} distance with the water coordination number of Mg^{2+} calculated from one WT-metaD trajectory. The PMF profile has a deep energy well at a P_i-Mg^{2+} distance of 3.4 Å with 3.2 waters coordinated with Mg^{2+}, indicating the most stable bound structure for P_i. Phosphate and Mg^{2+} dissociate above the high energy barrier at separations greater than 4.3 Å. At a coordination of ≥4.2 waters the coordination between P_i and Mg^{2+} breaks, allowing the separation of P_i and Mg^{2+}. This mechanism was observed in all simulated trajectories (**Supplementary Fig. S4**).

Stage 2, diffusion in the cavity. After leaving the nucleotide-binding site, P_i diffuses in a cavity (**Fig. 3B**), which we delinated by probing with a detection radius of 4.2 Å, comparable in size to phosphate (**Figures 3A** and **3B)**. ADP and Mg^{2+} occupy one end of the "C"-shaped cavity with the R177 gate at the other end (**Fig. 3B**). In between phosphate diffuses between the sensor loop (residues 71–77) and residues E107 and A108, where it can form hydrogen bonds with the backbone atoms of G74 and A108 (**Fig. 3C)**. The relatively flat free energy profile after the breaking the coordination between Mg^{2+} and P_i indicates a lack of strong interactions during this stage (**Fig. 1 (c)**).

Stage 2, diffusion in the cavity. After leaving the nucleotide-binding site, P_i diffuses in a cavity (**Fig. 3B**), which we delineated by probing with a detection radius of 4.2 Å, comparable in size to phosphate (**Figures 3A** and **3B)**. ADP and Mg^{2+} occupy one end of the "C"-shaped cavity with the R177 gate at the other end (**Fig. 3B**). In between phosphate diffuses between the sensor loop (residues 71–77) and residues E107 and A108, where it can form hydrogen bonds with the backbone atoms of G74 and A108 (**Fig. 3C)**. The relatively flat free energy profile after the breaking the coordination between Mg^{2+} and P_i indicates a lack of strong interactions during this stage (**Fig. 1C**).

Stage 3, opening the backdoor. To exit the actin subunit, P_i must overcome a second barrier thought to be formed at least in part by the side chain of R177. In cryo-EM structures (PDB 6DJN, 8A2S, 8D17), the side chain of R177 forms hydrogen bonds with the side chains of N111 and H161, and the backbone of P109, creating a barrier to P_i release **(Fig. 4A, Table 2)**. This has been called the R177 closed state. Crystal structures of actin monomers (34) and a cryo-EM structure of the pointed end of the ADP-actin filament (35) have the gate open with a salt bridge between R177 and the sidechain of D179 but no hydrogen bonds with N111 or P109 **(Fig. 4E, Table 2)**. This is the open state.

Our WT-MetaD and long unbiased MD simulations showed that the hydrogen-bonding interactions of R177 with HIC73, P109, N111, H161 and D179 fluctuate on a nanosecond (ns) time scale, visiting not only the open and closed states defined above but also multiple configurations that also block phosphate release without a hydrogen bond between R177 and N111 **(Figs. 4C-D, Table 2)**. We call these configurations occluded states. We used free energy profiles **(Fig. 5C)** to choose the cutoffs for the bonding distances to define four states of the phosphate gate based on distances between the side chains. The distance between two residues is determined as the distance between the closest pair of atoms involved in the formation of a hydrogen bond or a salt bridge. The specific atoms participating in these interactions can be found in Table 2, and a more detailed definition is provided in the Supplementary Materials. Trajectories of unbiased MD simulations show how the protein fluctuates among these three states: closed ⇆ occluded ⇆ open **(Figs. 5A-B)**.

Closed state: In the closed state, the distance between R177 and N111 ($D_{R177\text{-}N111}$) is < 3.53 Å and R177 also forms a hydrogen bond with the backbone of P109. **Fig. 4A** shows these hydrogen bonds and **Fig. 4B** shows that molecular surfaces occlude the channel for phosphate release.

Open state: The distances of R177 to its potential hydrogen-bonding partners are $D_{R177\text{-}P109}$ >3.8 Å, $D_{R177\text{-}HIC73}$ >3.57 Å, $D_{R177\text{-}H161}$ >3.66 Å and $D_{R177\text{-}D179}$ <3.40 Å **(Fig. 4E)**. Without a hydrogen bond between N111 and R177, N111 is reoriented to hydrogen bond with E107 and located further from R177, accounting for much of the separation. Thus, in the open state R177 forms a salt bridge with D179 but does not form hydrogen bonds with P109, H73 or H161 and leaves open the pore for phosphate to escape **(Fig. 4F and Supplementary Video 2)**.

Wide-open state: In this configuration with $D_{R177\text{-}N111}$ >13.7 Å and R177 forms a salt bridge with D179. In both the open and wide-open states the back door is open, creating a pore larger than the size of phosphate between the interior and exterior of the actin subunit **(Fig. 4F)**.

In our simulations P_i consistently moved towards the side chain of R177 as it exited from the protein and was fully released (**Fig. 4D** and **Supplementary Video 2)**. This is likely an electrostatic interaction between negatively charged P_i and positively charged R177 as shown by the charge distribution in **Fig. 4F**.

Occluded states: We define the occluded state as all configurations of the R177 hydrogen-bonding network other than the three states defined above. These include states with one or more rapidly fluctuating hydrogen-bonds between R177 and HIC73, P109 and/or H161 but not an electrostatic interaction with D179 (**Fig. 5C-D**). N111 forms a hydrogen bond with E107 rather than R177. Analysis of the molecular surfaces shows that the pathway for phosphate between the interior cavity and the exterior of the actin subunit is blocked **(Fig. 4B)**.

During both types of MD simulations starting in the occluded state, the occluded state is the most heavily populated. However, the subunits in available cryo-EM structures of filaments are either in the closed or open states **(Table 2)**.

To investigate whether freezing during preparation for cryo-EM might reconfigure the R177 hydrogen-bonding network, we changed the temperature during unbiased simulations. Starting in the closed state, lowering the temperature from 322°K to 77°K over 40 ns or alternating the temperature between 322° K to 77° K (a common strategy for finding states with minimal energy) did not change the hydrogen bonds of R177 **(Figs. 6B-C)**. Starting with the occluded state, the distance between R177 and N111 decreased **(Fig. 6D)**, indicating a transition towards the closed state. These simulations suggest that the closed state is more stable than the occluded state at lower temperatures and may explain the absence of the occluded state in frozen samples.

Additional occluded and wide-open states. Both types of MD simulations revealed a dynamic hydrogen-bonding network in the phosphate release channel giving rise to multiple metastable states that may be difficult to define based solely on cryo-EM structures and by inspection of that data. To search for overlooked or more obscure states we used a machine learning method called

state predictive information bottleneck (SPIB) (36) to identify metastable states automatically from the high-dimensional MD trajectories.

SPIB builds upon the Information Bottleneck (IB) principle (37) and aims to derive a concise yet informative representation of an input source with respect to a target variable. Notably, SPIB incorporates a dynamic learning process during training, enabling the acquisition of a discrete-state representation of the system. We calculated the pairwise distances between atoms from R177 and other residues (listed in **Table 3**) from the unbiased trajectories for use as the input for SPIB to learn the discrete-state representation.

SPIB defined not only the single closed and open states we identified based on cryo-EM structures, but also identified multiple substates corresponding to the occluded and wide-open states defined by our inspection **(Supplementary Table. S1)**. Specifically, SPIB state 1 closely matched our definition of the closed state, exhibiting the same hydrogen bond network. None of the SPIB states 3-6 had a hydrogen bond between R177 and N111 or the salt bridge between R177 and D179, so they align with our occluded conformations. SPIB states 8 and 9 defined by SPIB also agree with our definition of the wide-open conformation with the $D_{R177\text{-}N111}$ >13.7 Å and R177 forms a salt bridge with D179.

Two of the states identified by SPIB (2 and 7) were mixtures of conformations from two of our states. Among the conformations belonging to SPIB state 2, around half are the open state as we defined ($D_{R177\text{-}P109}$>3.8 Å, $D_{R177\text{-}HIC73}$ >3.57 Å, $D_{R177\text{-}H161}$ >3.66 Å and $D_{R177\text{-}D179}$ <3.40 Å). The other half of the SPIB state 2 conformations are occluded states. Similarly, in SPIB state 7 about half of the conformations belong in the occluded state, while the other half belong to the wide-open state. The fast transitions among these conformations may explain why SPIB groups them together in states 2 and 7.

Transitions among the four states of the gate. During long unbiased MD simulations, hydrogen bonds between R177 and formed and dissociated on a nanosecond time scale **(Figs. 5A, 5B)**. Transitions from the closed state to the open state and back always involve the occluded state as the intermediate. Thus, the closed state only transits to the occluded state. The occluded state is the most heavily populated and rarely transits to the closed or open state, so it dominates in blocking phosphate release. The open state is four times more likely to transit to the occluded

state than the wide-open state, while the wide-open state has similar probabilities of transiting to the open and the occluded state.

Discussion

The release of phosphate (P_i) from ADP-P_i-actin filaments is a critical step in the polymerization cycle of actin. We used enhanced free energy sampling methods and all-atom MD simulations to investigate the mechanism of P_i release from internal ADP-P_i subunits in actin filaments at the atomic level. We confirmed previous studies proposing a "back door" route for P_i release (4, 28) and characterized the energy barriers along the pathway. Our WT-MetaD and unbiased MD simulations revealed that P_i release is a three-step process involving two energy barriers and four main states of the release pathway.

Dissociation of phosphate from Mg^{2+}. The high barrier associated with dissociation of phosphate from Mg^{2+} determines the overall slow rate of the reaction. Initially, the change in coordination between Mg^{2+} and water molecules, along with the conformational changes near the nucleotide-binding site, destabilizes the interaction between Mg^{2+} and P_i, leading to the dissociation of P_i. This process makes the largest contribution to the overall PMF for the pathway and only occurs after disruption of the interaction between phosphate and Q137.

Experimentally, after hydrolysis, dissociation of inorganic phosphate proceeds at a rate of 0.003 s^{-1} (38) for interior subunits at room temperature. Assuming that subunit flattening increases ATP-hydrolysis 40,000 fold (6, 7), and subunits at the barbed end are progressively flattened as they acquire neighboring subunits (33), most of the phosphate release reactions occur in interior subunits at the barbed end. This slow rate implies an energy barrier of ~21 kcal/mol, assuming a transmission coefficient of unity in the Eyring transition state theory equation. In our simulations, an energy barrier of 20.5 ± 0.6 kcal/mol separates the P_i-Mg bound state from the P_i-Mg unbound state, the highest energy barrier during the release process. The agreement between this quantity and the experimentally derived energy barrier provides strong evidence that the breaking of coordination between Mg^{2+} and P_i is the rate-limiting step during P_i release. Other interactions in the active site accompany the dissociation of P_i from Mg^{2+}, including rearrangement of several residues to disrupt their interactions with P_i and the coordination between Mg^{2+} and water molecules. These factors collectively contribute to the high energy barrier in the PMF profile for the P_i release.

We were unable to simulate the reverse process, rebinding of P_i to the active site, due to the high entropy barrier that must be overcome. Therefore, we followed work using similar methods to study ligand unbinding (39-42), and refer to the free energy profiles obtained from these simulations as an approximate potential of mean force, PMF. Although specialized methods can be used to overcome this limitation (43), further research is needed to explore this possibility in-depth.

Mugnai and Thirumalai reported a stepwise hydration of Mg^{2+} in their simulation of phosphate release from a myosin motor and suggested that this is a universal mechanism to trigger the release of phosphate (44). In our simulations, the coordination number of water molecules around Mg^{2+} fluctuates on a relatively short time scale, but the release of P_i only occurs when four water molecules coordinate with the magnesium ion.

Internal movements of phosphate and fluctuations in the gate controlling phosphate release. After dissociation from Mg^{2+}, P_i diffuses through a channel near HIC73 in subdomain 1 (SD1) of the actin subunit, where it encounters a second, lower energy barrier associated with the transition of the R177 gate from the occluded state to the open state to release phosphate. The exit gate is closed or occluded most of the time, but when the protein fluctuates into the open state, P_i moves towards the R177 gate and dissociates from the protein. During four 1 μs unbiased MD simulations, the R177 gate opened multiple times (**Supplementary Fig. S5**).

We did not observe multiple transitions between all metastable states in the MD time courses in **Fig. 4**G, suggesting that none of these simulations achieved complete sampling of conformational probability of the backdoor gate. These dynamics are also reflected in the relatively low energy barrier for the final stage of the release process on the PMF profile (**Fig. 1D**). Therefore, opening and closing the backdoor gate may affect the relative rate of P_i release from the actin subunits in different confirmations along the filament but does not determine the overall slow rate of P_i release.

The occluded state revealed by our MD simulations dominates structure in the filament. In the occluded state, R177 does not hydrogen bond with N111, its partner in the closed state. Instead, R177 participates in a rapidly rearranging network of hydrogen bonds stabilizing conformations that block the pathway for phosphate to dissociate from actin. Remarkably, this state is not captured by current cryo-EM data. However, the occluded state may rearrange to the closed state during freezing.

Comparisons with other work. A preprint recently posted by Oosterheert et al. (45) reported MD simulations to investigate the mechanism of phosphate release from internal subunits in ADP-P_i-actin filaments. They used an enhanced sampling protocol to explore possible pathways of phosphate release and identified pathways with gates formed by R177 or R183. Using WT-MetaD, we found that the R177 backdoor pathway is the dominant pathway for P_i release, consistent with Oosterheert's mutagenesis and biochemical experiments and MD simulations of similar systems by others (28, 44). We did not observe phosphate trajectories toward R183, which may have been produced by conventional MetaD, depending on the reaction coordinates chosen (46). Incomplete sampling noted above may explain why shorter unbiased MD simulations reported by Oosterheert et al. did not sample the fully open state of the backdoor gate (45).

Oosterheert et al. also report the breaking the R177 and N111 hydrogen bond in shorter unbiased MD simulations, but the full opening of R177 was only observed in their steered MD simulation where they drove the configuration of the central subunit to the barbed-end configuration. Thus, the fully open state has a lower probability than other metastable states, but it is accessible by unbiased MD.

Oosterheert et al. reported a 3.6 Å resolution reconstruction of the barbed end of an ADP-actin filament with the backdoors on the internal subunits closed by hydrogen bonds between R177 and N111. However, rearrangement of the hydrogen bonding network of the terminal subunit left a 5 Å gap between residues N111 and R177, which may allow phosphate release. Instead, N111 interacts with E107.

It is noteworthy that we include a quantitative calculation of the large energy barrier for water-assisted dissociation of phosphate from Mg^{2}. This value agrees with the overall rate of phosphate release from actin filaments, so we conclude that it is the rate limiting step in the pathway. Oosterheert et al. did not calculate energy barriers, so they were unaware of this point and concluded "…the P_i release rate from F-actin is controlled by steric hindrance through the backdoor rather than by the disruption of the ionic bond between P_i and Mg^{2+} at the nucleotide-binding site."

Summary. Our study provides new insights into the mechanism of P_i release from actin filaments at an atomic level as well as a quantitative identification of the rate limiting step. Our findings may also have important implications for understanding how actin filaments function in

various cellular processes such as cell motility and cytokinesis. The results further demonstrate the ongoing value of enhanced sampling methods combined with all-atom MD simulations and machine learning for investigating complex biomolecular processes at the atomic level.

Methods and Materials

System and simulation setup

The system was constructed using a 5-mer section of interior subunits from the ADP-Pi 13-mer simulations performed in Zsolnay PNAS 2020 with an updated Charmm36m force field(47) and phosphate parameters generated with cgenff (48). To generate the 13-mer system in Zsolnay PNAS 2020, 13 ADP-P_i-F-actin subunits (PDB 6DJN) were patterned according to the rise and twist parameters reported in Chou & Pollard (PNAS 2019). The system was solvated using the autosolvate plugin in VMD (49) to add a TIP3P water box with a minimum separation of 11 Å between the protein and the periodic boundary. The autoionize plugin in VMD was used to neutralize the system and bring the solvent to a salt concentration of 100 mM KCl. The system was minimized, heated, and equilibrated with a series of constraints detailed in Zsolnay PNAS 2020. The system underwent a 320 ns unconstrained equilibration.

To construct the 5-mer system, five subunits from the interior of the 13-mer system (subunits 5 to 9) were selected after the unconstrained equilibration of 320 ns. All water molecules within 8 Å of the subunits were included in the selection. Autosolvate and autoionize were used to fill the remainder of the solvation box to guarantee a separation of 11 Å between the protein and the periodic boundary and a neutral system with 100 mM KCl. The initial structure was subjected to energy minimization and the minimization was terminated when the maximum force is smaller than 1000.0 kJ/mol/nm. After energy minimization, the system was equilibrated with an NPT ensemble for 10 ns with a 2 fs integration step. The Parrinello-Rahman barostat (50) and Bussi-Parrinello velocity rescaling thermostat (51) were used to simulate the constant NPT ensemble at temperature 310 K and pressure 1 bar. The conformations of the terminal subunits at both ends changed during this process.

All simulations used to study the release process were performed with the same constant NPT ensemble. Simulations were performed by using GROMACS 2020.4 compiled with PLUMED 2.4. The data generated from the simulations were analyzed by VMD(49), PyMol (52-54) and Python library MDanalysis(55, 56), and an in-house Python script.

We define the four subdomains of an actin molecule as: subdomain 1 (SD1): residues 1 to 32, 70 to 144, and 338 to 375; (SD2): residue 33 to 69; (SD3): residue 145 to 180, 270 to 337; (SD4): residue 181 to 269. The center of mass of the Cα atoms of each subdomain were used to compute a dihedral angle SD2-SD1-SD3-SD4.

Metadynamics simulation

The timescale for the release of P_i, which occurs over several minutes, is orders of magnitude longer than the timescale accessible through MD simulations, which typically run on the microsecond scale at best. To overcome this limitation and sample this rare event, we used WT-MetaD (29-32) to accelerate the release process. Unlike a conventional metadynamics (MetaD) simulation, which has convergence issues, WT-MetaD decreases the height of Gaussian bias according to the existing biasing potential and has demonstrated convergence properties(30, 49).

The choice of reaction coordinates is critical for the success of MetaD simulations. MetaD can enhance the sampling of rare events only when chosen reaction coordinates (or collective variables, CVs) provide a good representation of the process of interest. In this study, we employed two reaction coordinates to perform our WT-MetaD simulation: the distance between Mg^{2+} and the center of mass (COM) of P_i , denoted as $d_{Mg\text{-}Pi,}$ and the distance between the COM of the backbone R177 and the COM of $P_{i.}$ denoted as $d_{R177\text{-}Pi}$. The selection of these reaction coordinates was informed by both general intuition and previous studies of phosphate release. The cryo-EM structure indicates that the position of Mg^{2+} does not change after the release of P_i. Therefore, the distance between Mg^{2+} and P_i can be considered a good reaction coordinate as it indicates how far P_i is from its binding position. The equilibrium structure from an unbiased MD simulation presents a cavity inside the central actin subunit (Fig. 3). The cavity has the shape of a channel with the side chain R177 situated at its end in the closed state. It is natural to expect that after breaking the coordination with Mg^{2+}, P_i can diffuse in the cavity. Previous studies based on structure also indicate the important role of R177 in the release process. These factors motivated us to use the P_i-R177 distance, which is defined as the COM of P_i and the COM the backbone of R177, as the second RC. To make the RC less noisy, we only considered the backbone of R177 and avoided accounting for the fluctuation of its side chain.

To estimate the free energy profile (i.e., PMF), we took the approach suggested in Ref. (31) where the samples with microscopic coordinate R from WT-MetaD is each associated with a reweighting factor:

$$w(R) = e^{V(s(R),t)-c(t)} \tag{2}$$

Where $V(x)$ is the bias $c(t)$ is usually referred to as a time-dependent bias offset. The term $c(t)$ can be estimated "on the fly" in the MetaD using the form:

$$c(t) = \int ds\, [e^{\gamma V(s,t+\Delta t)/k_B T} - e^{\gamma V(s,t)/k_B T}] \tag{3}$$

where Δt is the time interval between successive bias depositions. The unbiased estimation of an observable can be calculated as:

$$\langle O(R)\rangle_{unbiased} = \frac{\langle O(R)w(R)\rangle_{biased}}{\langle w(R)\rangle_{biased}} \tag{4}$$

Next, the PMF can be calculated by $F(x) = -k_B T\, ln\langle\delta(x - x(R))\rangle_{unbiased}$. Noted that since here x can be any observable and is not necessary to be the reaction coordinate s, the free energy profiles of other variables of interest can also be obtained.

The choice of MetaD parameters of a WT-MetaD simulation includes the biasing factor, biasing frequency and bias height and the variance of the Gaussian bias. In our simulations, the biasing factor was set to be 10, the bias height was set to be 1 kcal/mol and the biasing frequency is set to be 5000 MD steps. These parameters were chosen to ensure that the biasing potential was not added too aggressively while still being able to accelerate the release process. The variances of Gaussian bias were set to be 0.05 Å and 0.5 Å separately for $d_{Pi\text{-}Mg}$ and $d_{Pi\text{-}R177}$ and these values were determined by half of the variance of these variables in a 50 ns unbiased MD simulation.

Acknowledgements

Research reported in this publication was supported by the National Institute of General Medical Sciences (NIGMS) of the National Institutes of Health (NIH) under award numbers R01GM026132 to TDP and R01GM063796 to GAV. YW gratefully acknowledges the support of Chicago Center for Theoretical Chemistry Fellowship and the Eric and Wendy Schmidt AI in Science Postdoctoral Fellowship. The content is solely the responsibility of the authors and does not necessarily represent the official views of the National Institutes of Health. The authors thank the University of Chicago Research Computing Center and the NIH-funded Beagle-3 computer (NIH award 1S10OD028655-01) for computational resources.

Tables

Table 1. Computer simulations performed in this study.

Simulation	Biasing method	Initial state	Number of simulations	Special Settings
P_i release without constrained subunits	WT-MetaD	Occluded state	6	-
P_i release with constrained terminal subunits	WT-MetaD, Harmonic restraint on the subunit dihedrals	Occluded state	4	-
Unbiased MD	-	Occluded state	4	-
Low temperature 1	-	Closed state	1	T=77 K
Low temperature 2	-	Closed state	1	Lowering the temperature from 322 K to 77 K
Low temperature 3	-	Closed state	1	Alternating the temperature between 322 K and 77 K
Low temperature 4	-	Occluded state	1	Alternating the temperature between 322 K and 77 K

Table 2. Distances between the sidechain of R177 and potential hydrogen-bonding partners in structures of actin monomers and filaments and in MD simulations. Measurements were taken from the following structures. Monomer: PDB 2V52. Internal: PDB 8A2T. P-1: Chou and Pollard https://biorxiv.org/cgi/content/short/2023.05.12.540494v1.

Filament subunits (except monomer)	Nucleo-tide	R177-N111 SC	R177-P109 C=O	R177-H161 SC	R177-H73 C=O	R177-D179 SC	Gate
Monomer	ATP	8.6 Å	6.6 Å	5.9 Å	4.8, 4.5 Å	3.2, 3.5 Å	Open
Internal	ADP	2.9, 3.0 Å	2.5 Å	7.2 Å	2.9 Å	3.8 Å	Closed
Pointed end P-1	ADP	9.6, 10.6Å	6.8 Å	5.5 Å	3.3 Å	3.0 Å	Open
MD closed	ADP-P_i	2.8 Å	2.8 Å	4.20 Å	3.5 Å	8.4 Å	Closed
MD occluded	ADP-P_i	8.2 Å	4.0 Å	5.1 Å	4.9 Å	7.4 Å	Occluded
MD open	ADP-P_i	10.3 Å	6.5 Å	7.3 Å	4.9 Å	2.79 Å	Open
MD wide-open	ADP-P_i	16.1 Å	10.8 Å	8.6 Å	9.9 Å	3.2 Å	Wide-open

---

Table 3. List of atoms that form the network of H-bonds around the phosphate release channel.

R177	**N111**	**P109**	**H161**	**H73**	**D179**
NNE	OD1	O	ND1	O	OD1
NH1	ND2		HE1		OD2
NH2					

Table 4. Transition probabilities between states. In each row are the probabilities of moving from the state represented by that row to the other states represented by the column.

	closed	occluded	open	wide-open
closed	0.96	0.04	0.0	0.0
occluded	0.0010	0.9883	0.008	0.002
open	0.0	0.116	0.857	0.028
wide-open	0.0	0.021	0.017	0.961

References

1. J. D. Rosenblatt, A. I. Lunt, D. J. Parry, T. A. Partridge, Culturing satellite cells from living single muscle fiber explants. *In Vitro Cellular & Developmental Biology - Animal* **31**, 773-779 (1995).
2. D. Drenckhahn, T. D. Pollard, Elongation of actin filaments is a diffusion-limited reaction at the barbed end and is accelerated by inert macromolecules. *Journal of Biological Chemistry* **261**, 12754-12758 (1986).
3. F. Merino *et al.*, Structural transitions of F-actin upon ATP hydrolysis at near-atomic resolution revealed by cryo-EM. *Nature Structural & Molecular Biology* **25**, 528-537 (2018).
4. S. Z. Chou, T. D. Pollard, Mechanism of actin polymerization revealed by cryo-EM structures of actin filaments with three different bound nucleotides. *Proceedings of the National Academy of Sciences* **116**, 4265-4274 (2019).
5. T. Oda, M. Iwasa, T. Aihara, Y. Maéda, A. Narita, The nature of the globular- to fibrous-actin transition. *Nature* **457**, 441-445 (2009).
6. L. Blanchoin, T. D. Pollard, Hydrolysis of ATP by Polymerized Actin Depends on the Bound Divalent Cation but Not Profilin. *Biochemistry* **41**, 597-602 (2002).
7. M. A. Rould, Q. Wan, P. B. Joel, S. Lowey, K. M. Trybus, Crystal Structures of Expressed Non-polymerizable Monomeric Actin in the ADP and ATP States*. *Journal of Biological Chemistry* **281**, 31909-31919 (2006).
8. M. McCullagh, M. G. Saunders, G. A. Voth, Unraveling the Mystery of ATP Hydrolysis in Actin Filaments. *Journal of the American Chemical Society* **136**, 13053-13058 (2014).
9. R. Sun, O. Sode, J. F. Dama, G. A. Voth, Simulating Protein Mediated Hydrolysis of ATP and Other Nucleoside Triphosphates by Combining QM/MM Molecular Dynamics with Advances in Metadynamics. *Journal of Chemical Theory and Computation* **13**, 2332-2341 (2017).
10. H. Freedman, T. Laino, A. Curioni, Reaction Dynamics of ATP Hydrolysis in Actin Determined by ab Initio Molecular Dynamics Simulations. *Journal of Chemical Theory and Computation* **8**, 3373-3383 (2012).
11. J. Akola, R. O. Jones, Density Functional Calculations of ATP Systems. 2. ATP Hydrolysis at the Active Site of Actin. *The Journal of Physical Chemistry B* **110**, 8121-8129 (2006).
12. R. Glaves, G. Mathias, D. Marx, Mechanistic Insights into the Hydrolysis of a Nucleoside Triphosphate Model in Neutral and Acidic Solution. *Journal of the American Chemical Society* **134**, 6995-7000 (2012).
13. N. V. Plotnikov, B. R. Prasad, S. Chakrabarty, Z. T. Chu, A. Warshel, Quantifying the Mechanism of Phosphate Monoester Hydrolysis in Aqueous Solution by Evaluating the Relevant Ab Initio QM/MM Free-Energy Surfaces. *The Journal of Physical Chemistry B* **117**, 12807-12819 (2013).
14. J. Akola, R. O. Jones, ATP Hydrolysis in Water − A Density Functional Study. *The Journal of Physical Chemistry B* **107**, 11774-11783 (2003).
15. M. J. McGrath, I. F. W. Kuo, S. Hayashi, S. Takada, Adenosine Triphosphate Hydrolysis Mechanism in Kinesin Studied by Combined Quantum-Mechanical/Molecular-Mechanical Metadynamics Simulations. *Journal of the American Chemical Society* **135**, 8908-8919 (2013).

16. A. Jégou *et al.*, Individual Actin Filaments in a Microfluidic Flow Reveal the Mechanism of ATP Hydrolysis and Give Insight Into the Properties of Profilin. *PLOS Biology* **9**, e1001161 (2011).
17. H. Isambert *et al.*, Flexibility of actin filaments derived from thermal fluctuations. Effect of bound nucleotide, phalloidin, and muscle regulatory proteins. *Journal of Biological Chemistry* **270**, 11437-11444 (1995).
18. A. Orlova, E. H. Egelman, A Conformational Change in the Actin Subunit Can Change the Flexibility of the Actin Filament. *Journal of Molecular Biology* **232**, 334-341 (1993).
19. J.-W. Chu, G. A. Voth, Allostery of actin filaments: Molecular dynamics simulations and coarse-grained analysis. *Proceedings of the National Academy of Sciences* **102**, 13111-13116 (2005).
20. J.-W. Chu, G. A. Voth, Coarse-Grained Modeling of the Actin Filament Derived from Atomistic-Scale Simulations. *Biophysical Journal* **90**, 1572-1582 (2006).
21. J. Pfaendtner, E. Lyman, T. D. Pollard, G. A. Voth, Structure and Dynamics of the Actin Filament. *Journal of Molecular Biology* **396**, 252-263 (2010).
22. T. D. Pollard, Regulation of Actin Filament Assembly by Arp2/3 Complex and Formins. *Annual Review of Biophysics and Biomolecular Structure* **36**, 451-477 (2007).
23. T. D. Pollard, Actin and Actin-Binding Proteins. *Cold Spring Harbor Perspectives in Biology* **8** (2016).
24. B. Mehrafrooz, A. Shamloo, Mechanical differences between ATP and ADP actin states: A molecular dynamics study. *Journal of Theoretical Biology* **448**, 94-103 (2018).
25. J. Pfaendtner, D. Branduardi, M. Parrinello, T. D. Pollard, G. A. Voth, Nucleotide-dependent conformational states of actin. *Proceedings of the National Academy of Sciences* **106**, 12723 (2009).
26. W. Oosterheert, B. U. Klink, A. Belyy, S. Pospich, S. Raunser, Structural basis of actin filament assembly and aging. *Nature* **611**, 374-379 (2022).
27. M. J. Reynolds, C. Hachicho, A. G. Carl, R. Gong, G. M. Alushin, Bending forces and nucleotide state jointly regulate F-actin structure. *Nature* **611**, 380-386 (2022).
28. W. Wriggers, K. Schulten, Investigating a back door mechanism of actin phosphate release by steered molecular dynamics. **35**, 262-273 (1999).
29. A. Barducci, G. Bussi, M. Parrinello, Well-Tempered Metadynamics: A Smoothly Converging and Tunable Free-Energy Method. *Physical Review Letters* **100**, 020603 (2008).
30. J. F. Dama, M. Parrinello, G. A. Voth, Well-Tempered Metadynamics Converges Asymptotically. *Physical Review Letters* **112**, 240602 (2014).
31. P. Tiwary, M. Parrinello, A Time-Independent Free Energy Estimator for Metadynamics. *The Journal of Physical Chemistry B* **119**, 736-742 (2015).
32. O. Valsson, P. Tiwary, M. Parrinello, Enhancing Important Fluctuations: Rare Events and Metadynamics from a Conceptual Viewpoint. *Annual Review of Physical Chemistry* **67**, 159-184 (2016).
33. V. Zsolnay, H. H. Katkar, S. Z. Chou, T. D. Pollard, G. A. Voth, Structural basis for polarized elongation of actin filaments. *Proceedings of the National Academy of Sciences* **117**, 30458-30464 (2020).
34. S. Mouilleron, S. Guettler, C. A. Langer, R. Treisman, N. Q. McDonald, Molecular basis for G-actin binding to RPEL motifs from the serum response factor coactivator MAL. *The EMBO Journal* **27**, 3198-3208 (2008).

35. Z. C. Steven, D. P. Thomas, Cryo-EM structures of both ends of the actin filament explain why the barbed end elongates faster than the pointed end. *bioRxiv* 10.1101/2023.05.12.540494, 2023.2005.2012.540494 (2023).
36. D. Wang, P. Tiwary, State predictive information bottleneck. *The Journal of Chemical Physics* **154**, 134111 (2021).
37. N. Tishby, F. C. Pereira, W. Bialek, The information bottleneck method. *arXiv [physics.data-an]* (2000).
38. R. Melki, S. Fievez, M.-F. Carlier, Continuous Monitoring of Pi Release Following Nucleotide Hydrolysis in Actin or Tubulin Assembly Using 2-Amino-6-mercapto-7-methylpurine Ribonucleoside and Purine-Nucleoside Phosphorylase as an Enzyme-Linked Assay. *Biochemistry* **35**, 12038-12045 (1996).
39. G. Saladino, L. Gauthier, M. Bianciotto, F. L. Gervasio, Assessing the Performance of Metadynamics and Path Variables in Predicting the Binding Free Energies of p38 Inhibitors. *Journal of Chemical Theory and Computation* **8**, 1165-1170 (2012).
40. P. Tiwary, J. Mondal, B. J. Berne, How and when does an anticancer drug leave its binding site? *Science Advances* **3**, e1700014.
41. H. Vashisth, C. F. Abrams, Ligand Escape Pathways and (Un)Binding Free Energy Calculations for the Hexameric Insulin-Phenol Complex. *Biophysical Journal* **95**, 4193-4204 (2008).
42. Y. Wang, S. Parmar, J. S. Schneekloth, P. Tiwary, Interrogating RNA–Small Molecule Interactions with Structure Probing and Artificial Intelligence-Augmented Molecular Simulations. *ACS Central Science* **8**, 741-748 (2022).
43. R. Capelli, P. Carloni, M. Parrinello, Exhaustive Search of Ligand Binding Pathways via Volume-Based Metadynamics. *The Journal of Physical Chemistry Letters* **10**, 3495-3499 (2019).
44. M. L. Mugnai, D. Thirumalai, Step-Wise Hydration of Magnesium by Four Water Molecules Precedes Phosphate Release in a Myosin Motor. *The Journal of Physical Chemistry B* **125**, 1107-1117 (2021).
45. W. Oosterheert *et al.*, Molecular mechanisms of inorganic-phosphate release from the core and barbed end of actin filaments. *bioRxiv* 10.1101/2023.03.25.534205, 2023.2003.2025.534205 (2023).
46. J. M. L. Ribeiro, S.-T. Tsai, D. Pramanik, Y. Wang, P. Tiwary, Kinetics of Ligand–Protein Dissociation from All-Atom Simulations: Are We There Yet? *Biochemistry* **58**, 156-165 (2019).
47. J. Huang *et al.*, CHARMM36m: an improved force field for folded and intrinsically disordered proteins. *Nature Methods* **14**, 71-73 (2017).
48. K. Vanommeslaeghe *et al.*, CHARMM general force field: A force field for drug-like molecules compatible with the CHARMM all-atom additive biological force fields. *Journal of Computational Chemistry* **31**, 671-690 (2010).
49. W. Humphrey, A. Dalke, K. Schulten, VMD: Visual molecular dynamics. *Journal of Molecular Graphics* **14**, 33-38 (1996).
50. G. Bussi, M. Parrinello, Accurate sampling using Langevin dynamics. *Physical Review E* **75**, 056707 (2007).
51. H. J. C. Berendsen, J. P. M. Postma, W. F. van Gunsteren, A. DiNola, J. R. Haak, Molecular dynamics with coupling to an external bath. *The Journal of Chemical Physics* **81**, 3684-3690 (1984).

52. L. L. C. Schrödinger (2015) The AxPyMOL Molecular Graphics Plugin for Microsoft PowerPoint, Version 1.8.
53. L. L. C. Schrödinger (2015) The JyMOL Molecular Graphics Development Component, Version 1.8.
54. L. L. C. Schrödinger (2015) The PyMOL Molecular Graphics System, Version 1.8.
55. N. Michaud-Agrawal, E. J. Denning, T. B. Woolf, O. Beckstein, MDAnalysis: A toolkit for the analysis of molecular dynamics simulations. *Journal of Computational Chemistry* **32**, 2319-2327 (2011).
56. R. J. Gowers *et al.*, MDAnalysis: A Python Package for the Rapid Analysis of Molecular Dynamics Simulations. 10.25080/Majora-629e541a-00e (2019).

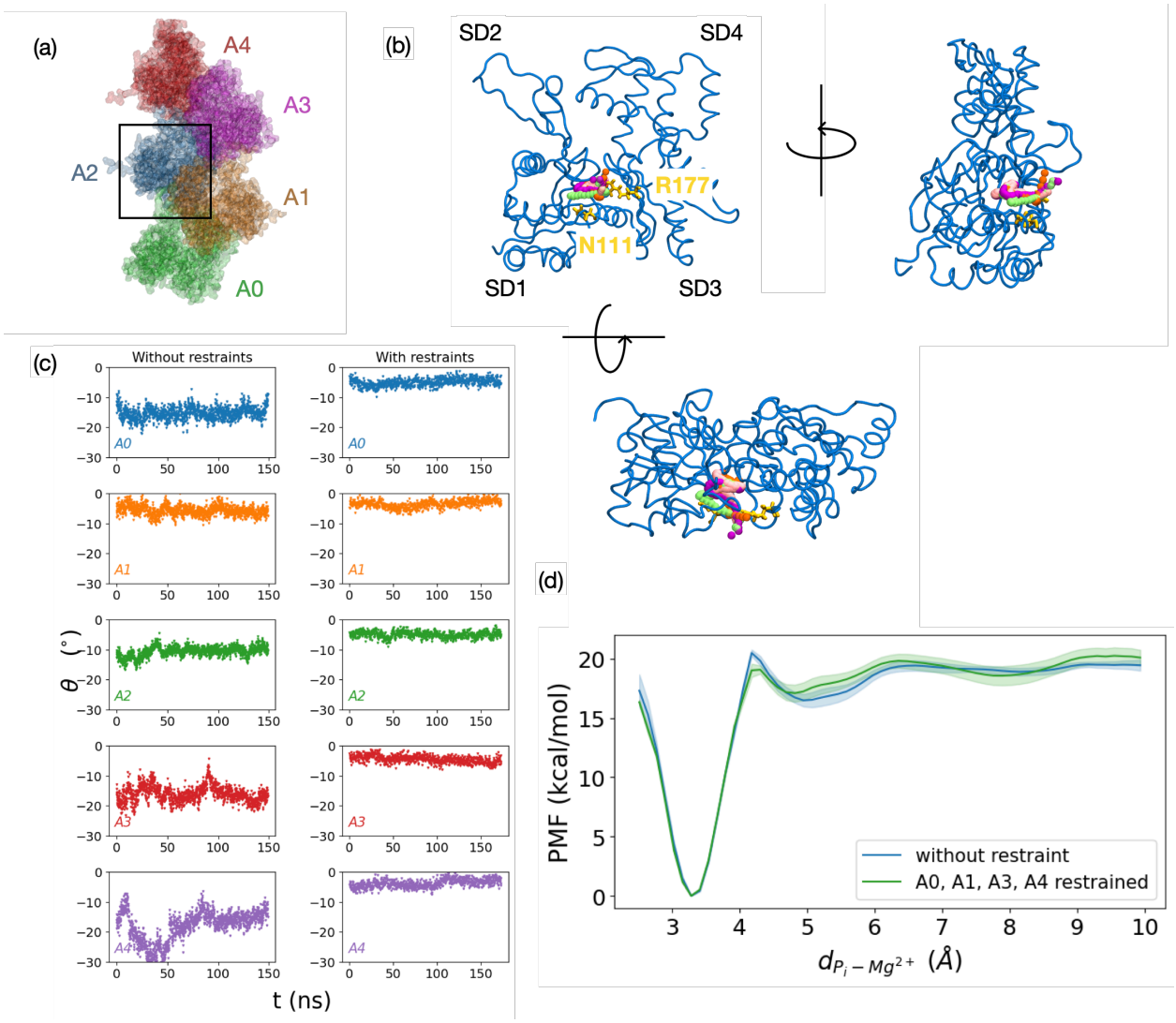

Fig. 1. Pathways of P_i release in independent WT-MetaD simulations. A. Cartoon representation of the actin filament 5-mer with the subunits colored in green, orange, blue, purple and red from A0 to A4. B, Four trajectories of phosphate release (green, pink, purple and orange) from actin subunit A2 (blue backbone trace) made by plotting the positions of the phosphorus in each frame. R177 and N111 (yellow) indicate the exit of the "backdoor" pathway. C. Time course of the subunit dihedral angles in WT-metaD simulations with unrestrained simulations in the left column and restrained simulations in the right column with a force constant of 5000 kJ/mol/radian2 applied on subunits A0, A1, A2 and A4. D, Potential of mean force (PMF) as a function of the distance between phosphate and the Mg^{2+} ion from the constrained (green) and unconstrained (blue) simulations. The shaded region are standard errors.

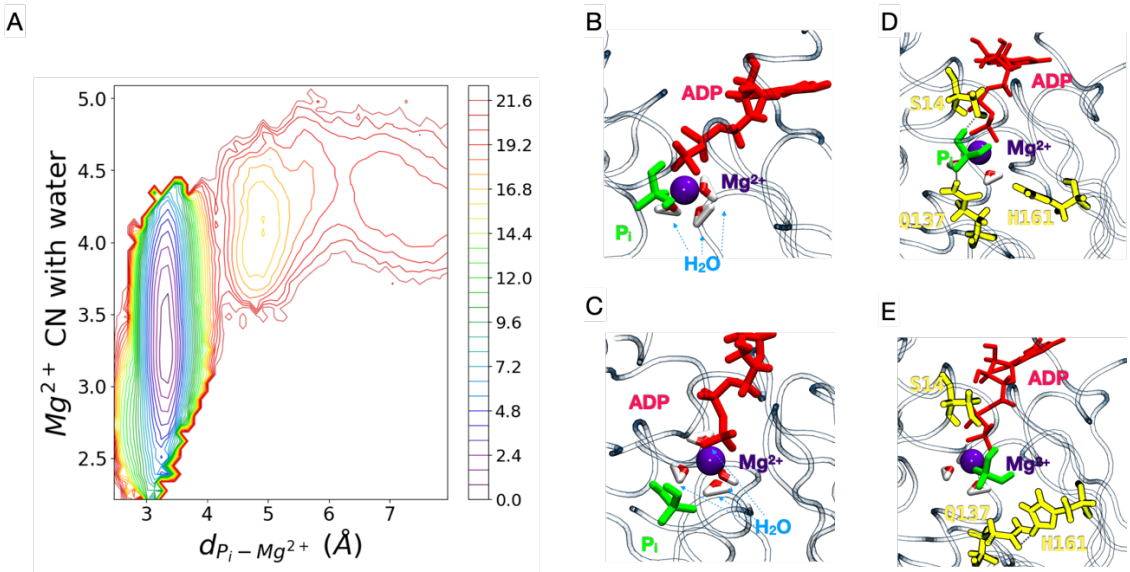

Fig. 2. The release of P_i proceeds with the solvation of Mg^{2+} and the disruption of nearby residue interactions near the active site. Mg^{2+} is depicted as a purple sphere using the VDW presentation with a 0.8 scale. A. A 2-dimensional PMF is shown as a function of Mg^{2+} coordination number with water and the P_i-Mg^{2+} distance calculated from one release trajectories (See Supplementary Material for PMFs from other trajectories). B-C. Structures at two time points during a WT-MetaD simulation. ADP (red) and P_i (green) are plotted using the licorice representation. B. Mg^{2+} is coordinated with 3 water molecules. C. Mg^{2+} coordinated with 4 water molecules. D. P_i hydrogen-bonds with the oxygen of the side chain of residue S14 and a hydrogen atom of the side chain amine group of residue Q137. All residues are shown in the licorice representation and colored in yellow. E. After Q137 changes its rotameric position, a hydrogen bond forms between the oxygen in its side chain and a hydrogen on the ring of H161. During our MD simulations this change always occurs before P_i loses its coordination with Mg^{2+} (see Supplementary Materials for more details).

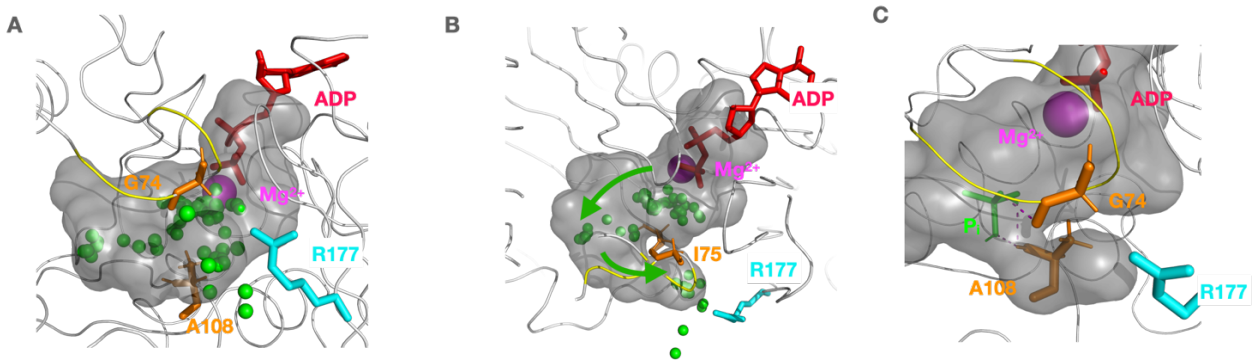

Fig. 3. P_i diffuses in a cavity inside an actin subunit between the active site and the R177 back door in the occluded state. The cavity is shown as a grey surface defined by probing an equilibrium structure from an unbiased MD simulation in the occluded state with a detection radius of 4.2 Å. Mg^{2+} is shown as a purple sphere, ADP (red), R177 (blue), G74 (orange) A108 (orange) are shown in the licorice representation. The phosphorus atom of the P_i is plotted in green spheres at different times selected to distribute the spheres uniformly in space. A-B, cavity from two viewpoints in the occluded state with green arrows to indicate the direction of the release process. C. The hydrogen bonds (purple dash lines) form between P_i and the backbone carbonyl oxygen of residue G74 or the amide hydrogen of residue A108.

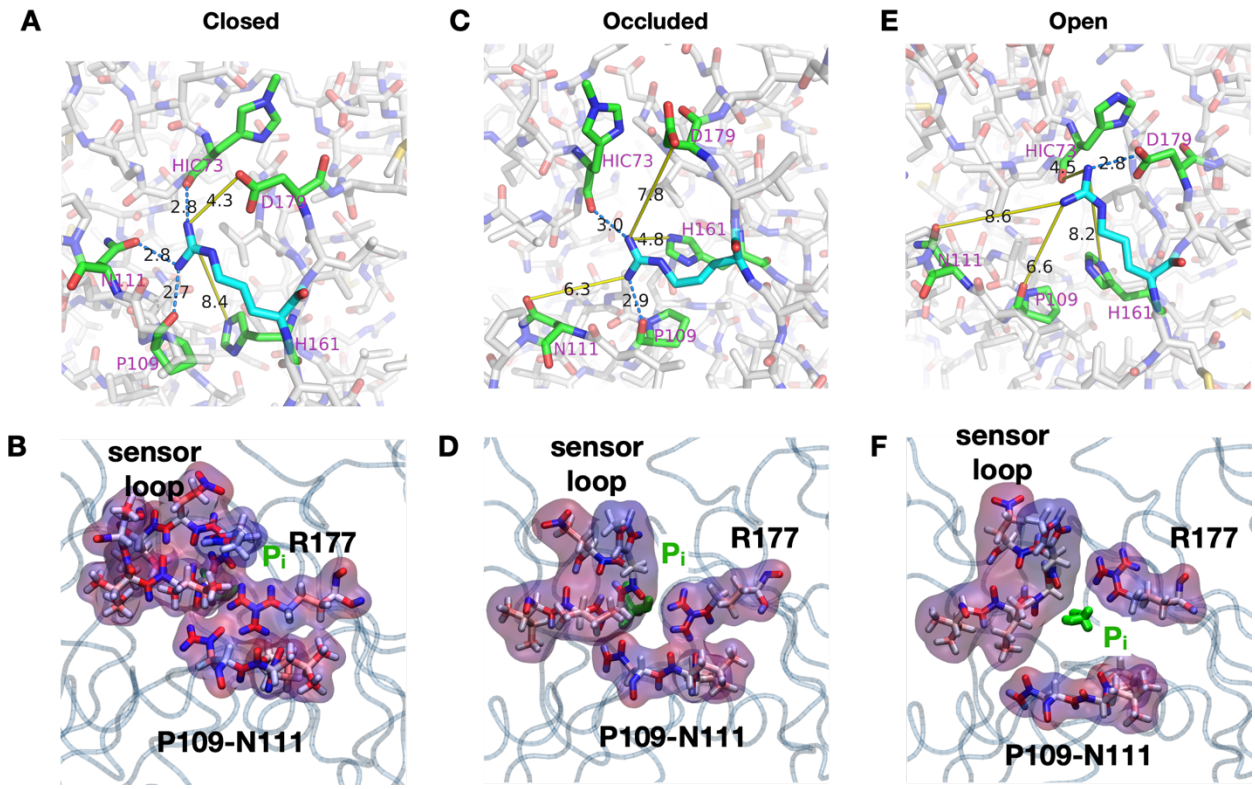

Fig. 4. Hydrogen bonding networks of R177 in the (A-B) closed state, (C-D) occluded state and (D-E) open state. The top row shows stick figures with hydrogen bonds as blue dotted lines and longer distances to potential hydrogen bond partners as yellow lines. The second row shows surface representations of the residues forming the gate in MD simulations. The surfaces of the sensor loop (residues 71 to 77), R177, N111, and P109 are colored by the charge density with red for positive charges and blue for negative charges. A, Cryo-EM structure of ADP-P_i-actin filaments (PDB 8A2S) with a hydrogen bonds between R177 and the sidechain of N111as well as the backbones of HIC73 and P109 closing the gate. B, Surface representation of the closed state in an MD simulation. C-D, Snapshots from an unbiased MD simulation in the occluded state. R177 hydrogen bonds with the backbone of P109 and the side chain of H161 precluding the release of phosphate. E-F, Open state with an electrostatic interaction between the sidechains of R177 and D179 that opens a channel for phosphate to escape. E, Crystal structure of MAL-RPEL2 complexed to G-actin (PDB 2V52) in the open state. F, Snapshot from a WT-MetaD simulation in the open state.

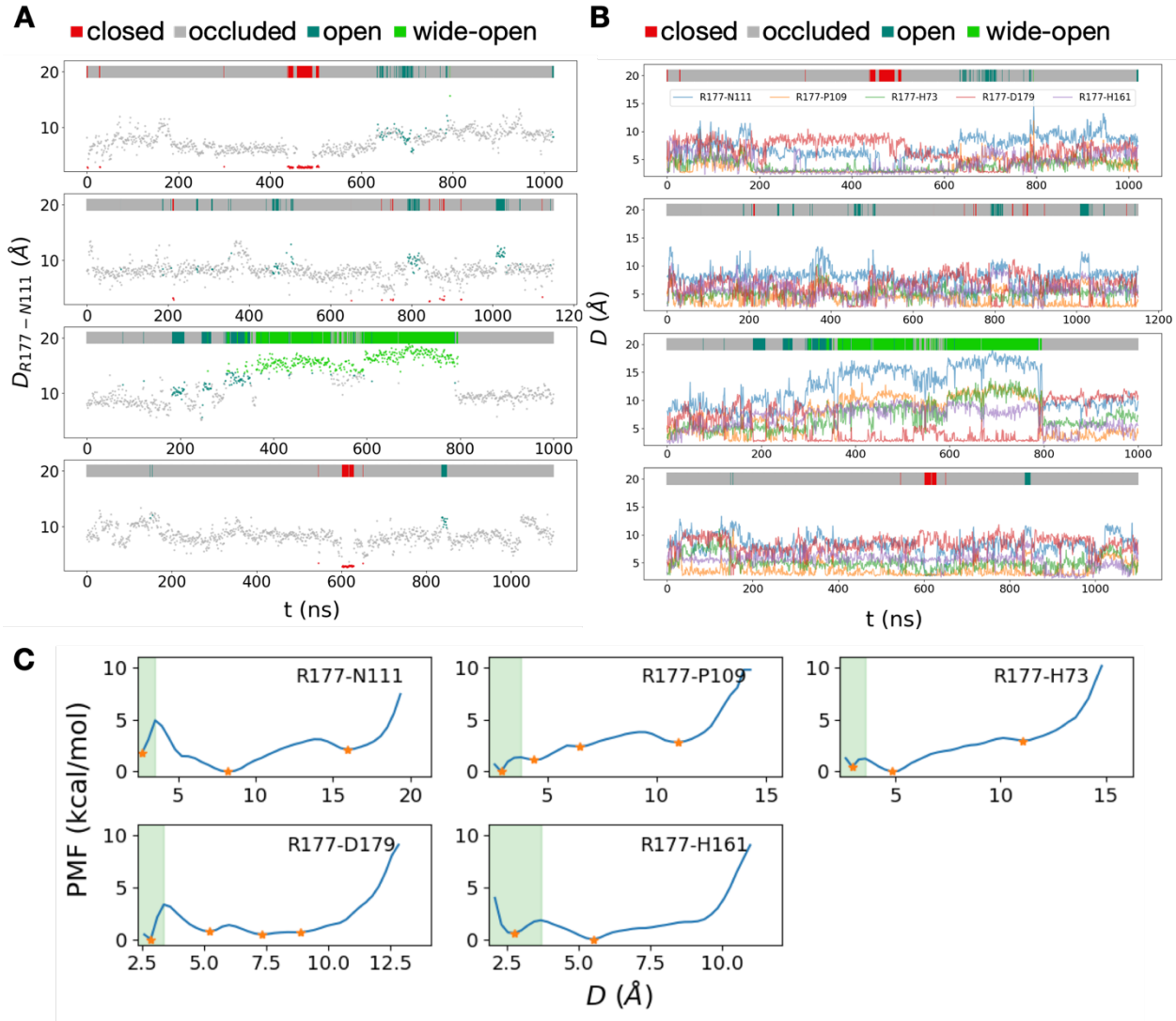

Fig. 5. A-B, Distances between R177 and its hydrogen bonding partners at 1 ns intervals in four unbiased MD trajectories. The colors of individual data points and the bars at the top of each panel indicate the four states, closed (red), occluded (grey), open (acqua) and wide-open (green). A, R177-N111. B, Distances between the sidechain of R177 and the sidechains of N111, H161 and D179 and the backbones of HIC73 and P109. C, Free energies vs. distances between R177 and residues with which it forms hydrogen-bonds. Orange stars indicate energy basins, and green shaded areas depict regions where hydrogen bonds or salt bridges form between corresponding residue pairs. The energy profiles depend on the distinct chemical properties of the residues and their surrounding environments. For example, the R177-N111 distance has three distinct basins in the energy landscape. The basin around 2.5 Å, is associated with the hydrogen bond between R177 and N111. The other basins at 8.5 Å and 16.0 Å represent interactions that stabilize the system such as hydrogen bonds with other residues.

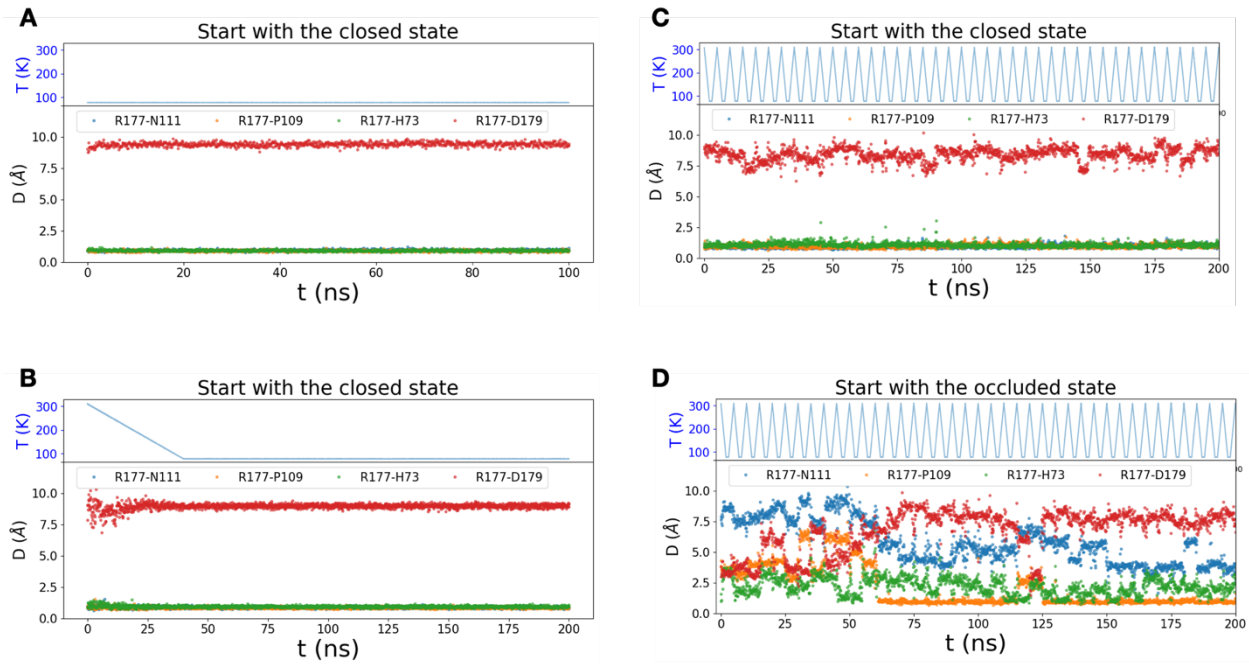

Fig. 6. Unbiased MD simulations employing various temperature schemes. A, Starting with the closed state the temperature was maintained at 77 K throughout the simulation. B, Starting with the closed state the temperature gradually decreased from 322 K to 77 K over the initial 40 ns and remained constant at 77° K thereafter. C-D, The temperature was alternated periodically using a a linear decrease from 322 K to 77 K over 2 ns, followed by a constant temperature of 77 K for 1 ns, before a linear increase back to 322 K over 2 ns. C, Starting with the closed state. D, Starting with the occluded state. The backdoor gate remained closed state with the temperature schemes in A-C and tended from the occluded state toward the closed state in D.

Title: **Mechanism of Phosphate Release from Actin Filaments**

Yihang Wang[a], Vilmos Zsolnay,[b] Thomas D. Pollard,[c,d,e,*] and Gregory A. Voth[a,1]

[a]Department of Chemistry, Chicago Center for Theoretical Chemistry, Institute for Biophysical Dynamics and James Frank Institute, University of Chicago, Chicago, IL

[b]Graduate Program in Biophysical Sciences, University of Chicago, Chicago, IL

Department of Molecular Cellular and Developmental Biology, Yale University, New Haven, CT

Department of Molecular Biophysics and Biochemistry, Yale University, New Haven, CT

Department of Cell Biology, Yale University, New Haven, CT

*Current address: Department of Cell and Molecular Biology, University of California, Berkeley

Supplemental materials

Supporting Information Text

Water coordination number

The water coordination number of Mg^{2+} is calculated using a switch function and has the form:

$$c = \frac{1}{3}\sum_{i\in W}\frac{1-\left(\frac{r_i}{r_0}\right)^6}{1-\left(\frac{r_i}{r_0}\right)^{12}}$$

Here r_0 is set to be 3 Å and the summation is over all atoms of water molecules.

Distance between residues

H-bonds can form between distinct atom pairs from two residues during the course of a simulation. To characterize the H-bonds networks between residues, we monitored the smallest distance between atoms that participate in forming hydrogen and electrostatic bonds. The distance between two residues I and J reported in our study is defined by:

$$\boldsymbol{D_{I-J}} = \min_{i\in I, j\in J} \boldsymbol{d_{i-j}}$$

Where $\boldsymbol{d_{i-j}}$ is the distance between atom i and j, which belong to residue I and J separately and participate in forming H-bonds (listed in Table 2).

Transition probability between different conformations of backdoor gate

To estimate the transition probability between states, we first label each frame according to our definition of the open, occluded, open and wide-open states. Then, we went through four unbiased trajectories and counted the number of transitions between states. Then the number of transitions is recorded as element of transition matrix T. To obtain probabilities, we normalize the matrix by dividing each element in the transition matrix by the total count of transitions from the corresponding state. This step ensures that the matrix represents a valid probability distribution.

State Predict Information Bottleneck

SPIB utilizes a neural network with an encoder and decoder structure to effectively cluster the high-dimensional MD trajectories into metastable states. The neural network is trained to extract only the essential information from past trajectories, which is crucial for accurately predicting the future state of the system. During the training process, the network learns a discrete-state representation, focusing specifically on the motion associated with state-to-state transitions.

For our specific implementation, we selected a deep neural network as the encoder to effectively capture the nonlinear relationship among the input variables. The training dataset comprised 24 pairwise distances between atoms involved in forming the H-bond network around R177. Default hyperparameters were employed, and a time delay of 3 ns was chosen to filter out fast dynamic.

Initial Structure Preparation for constrained simulations

We used Steered-MD (SMD) to create the initial structures for constrained simulations, with all subunit dihedral angles being driven to -3°. We first applied harmonic restraints with a force constant of 5000 kJ/mol/radian^2 on the dihedral angles of all subunits. The center of harmonic restraints moves to -3.01 radians in 10 ns with a constant velocity. Then we fixed the centers of harmonic restraints and linearly decreased or increased the force constant between 5000 kJ/mol/radian^2 and 100 kJ/mol/radian^2 with a 20 ns period. This relaxation process helped the system better find the local minimum. Fig. S6 shows how the center and the force constant change during the simulation of preparing the initial structure. After the SMD simulations, the restraint on the central subunit was removed, and a 100 ns simulation was initialized to further equilibrate the system. The initial structure was picked from the frame with the central unit dihedral angle being closest to -3° during the last equilibrium phase.

Supplemental Table

Table S1. SPIB analysis of unbiased MD simulations: learned states and average distances (Å) between R177 and interacting residues. Red font indicates distances short enough to form hydrogen or electrostatic bonds. See Fig. S1 for time courses.

SPIB state	R177-N111 SC	R177-P109 C=O	R177-H161 SC	R177-H73 C=O	R177-D179 SC	Gate
1	2.8	2.8	3.9	3.1	8.70	Closed
2	10.3	5.64	6.5	6.14	6.0	Mixture of open and occluded
3	8.2	4.2	5.5	4.9	7.0	Occluded
4	6.0	2.8	2.9	3.0	7.5	Occluded
5	9.5	3.9	4.7	6.4	10.5	Occluded
6	8.2	3.4	5.6	7.8	9.5	Occluded
7	13.6	9.0	8.2	7.6	4.5	Mixture of occluded and wide-open
8	14.7	9.9	8.5	7.6	3.0	Wide-open
9	16.8	11.3	8.5	11.2	3.1	Wide-open

Supplemental figures

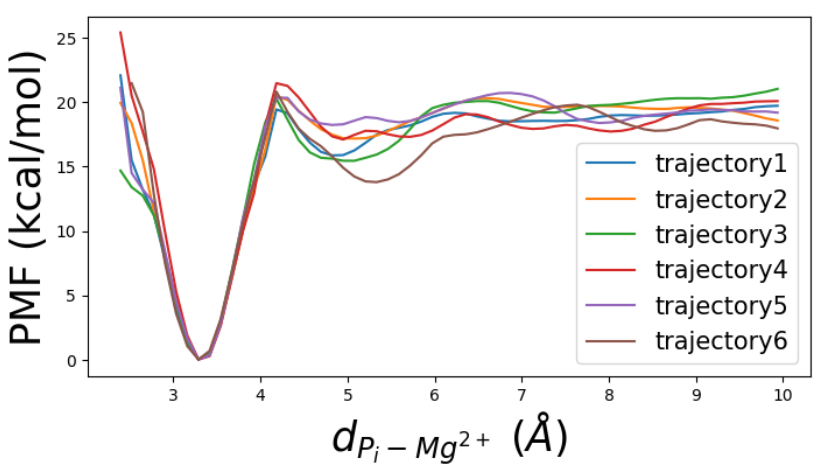

Fig. S1. The potential of mean force (PMF) profiles from six independent WT-MetaD trajectories. The low variance across the simulations suggests the release pathway is robust.

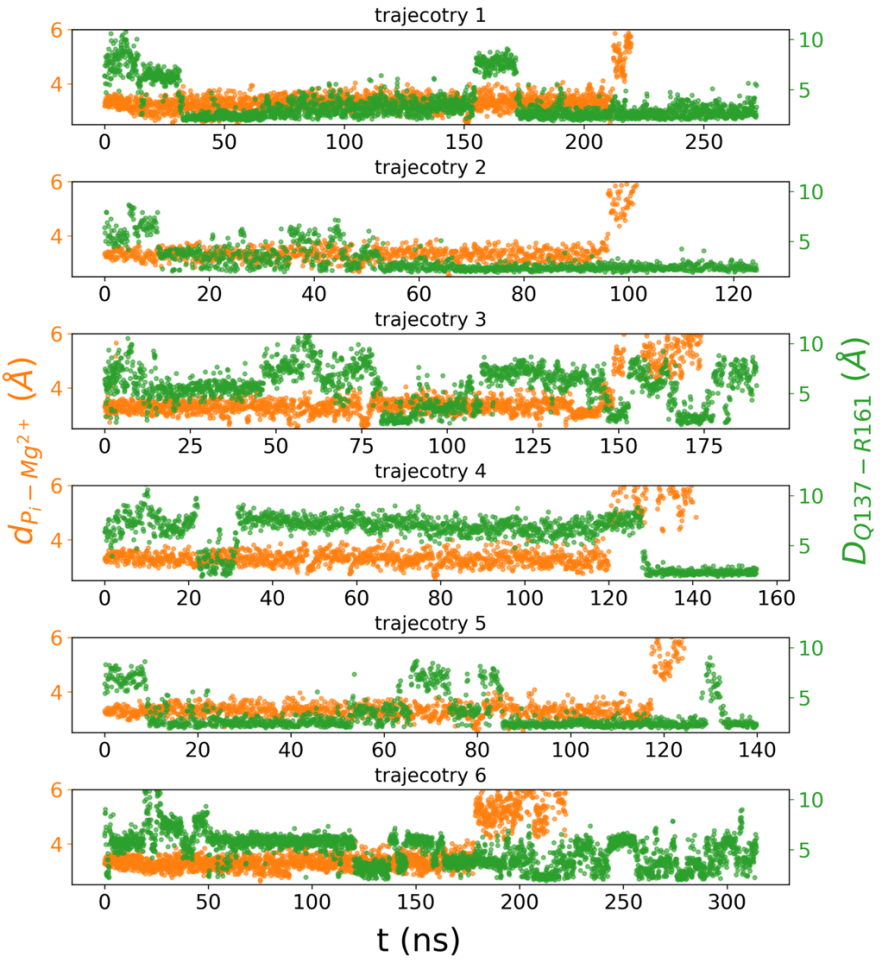

Fig. S2, Time courses from six independent WT-MetaD simulations of distances between phosphate and Mg^{2+} (orange) and between the atoms of Q137 and H161 that can form a hydrogen bond (green). Phosphate separates from Mg^{2+} only after Q137 reorients away from P_i to form a hydrogen bond with the side chain of H161. See Fig. 2D, E for visualization of the rearrangement of Q137.

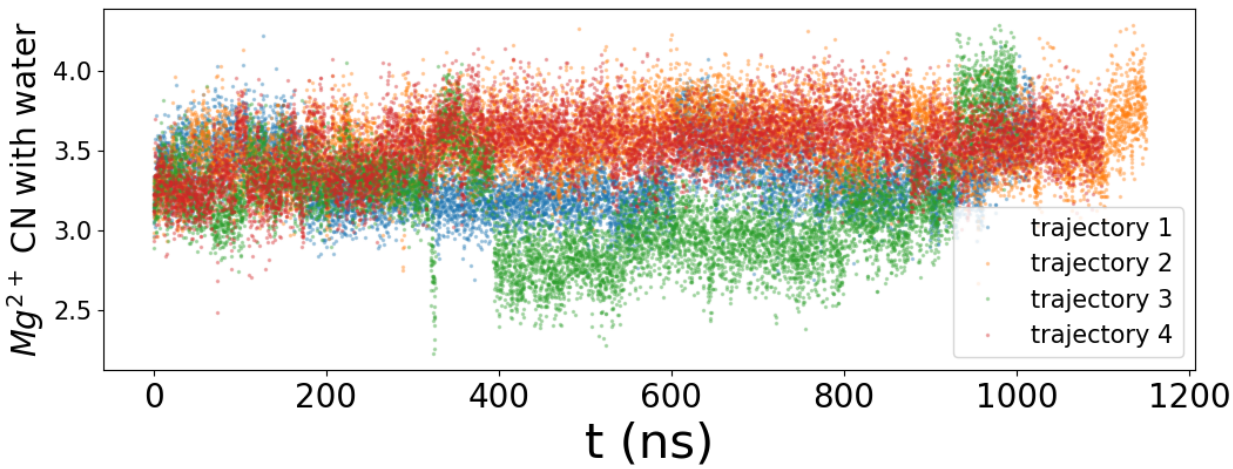

Fig. S3. Time courses from three independent unbiased MD simulations of the number of waters coordinated with Mg^{2+}. The number fluctuates between 2.3 to 4 over time. See Fig. 2B,C for visualization of the waters in the active site.

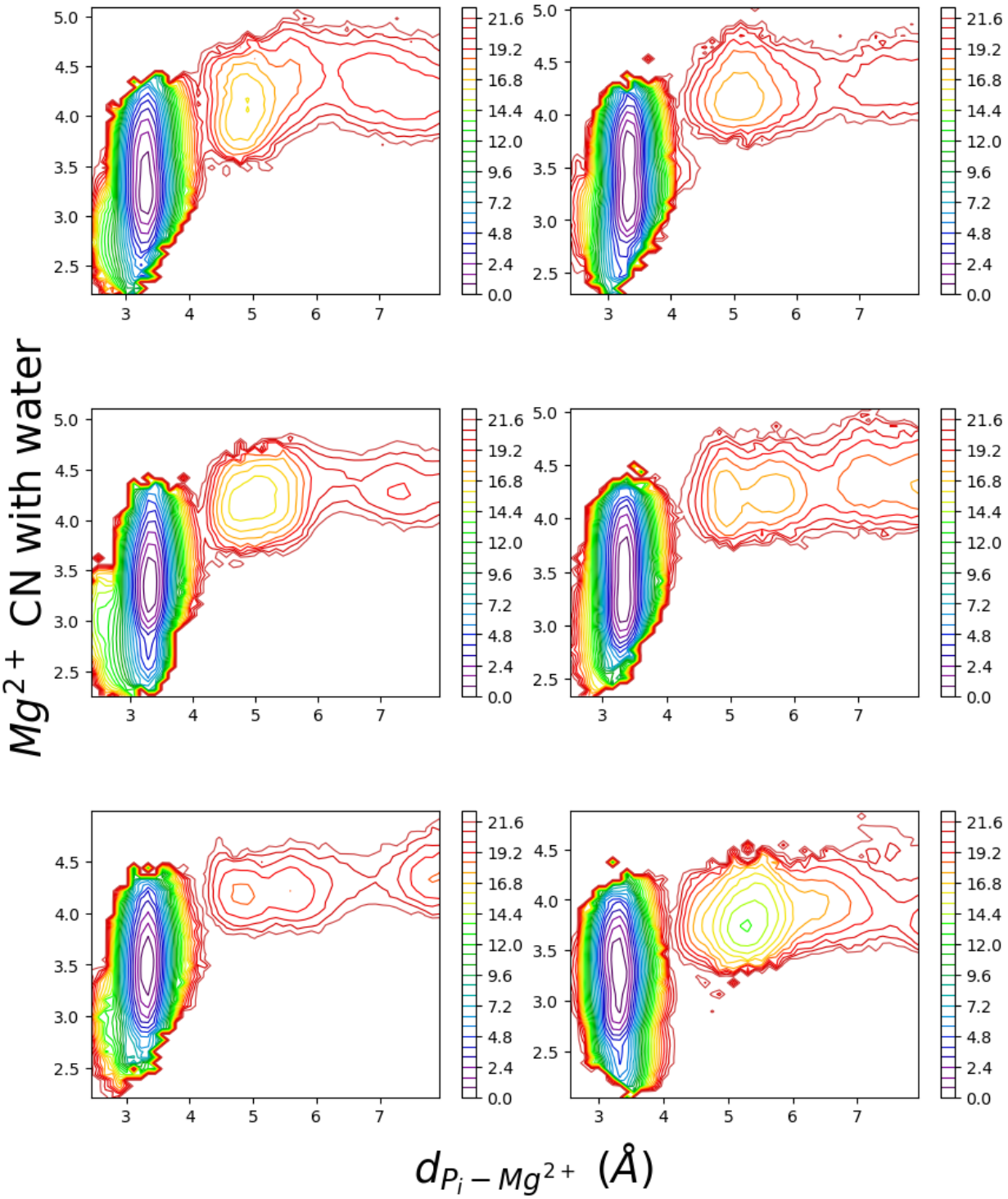

Fig. S4. Two-dimensional potential of mean force (PMF; i.e., colored coded free energy contours) from six independent WT-MetaD trajectories as a function of the number of waters coordinated with Mg^{2+} and the distance between P_i and Mg^{2+}. Phosphate separates from Mg^{2+} only after four waters coordinate with Mg^{2+}. The upper left panel is the same as Fig. 2A.

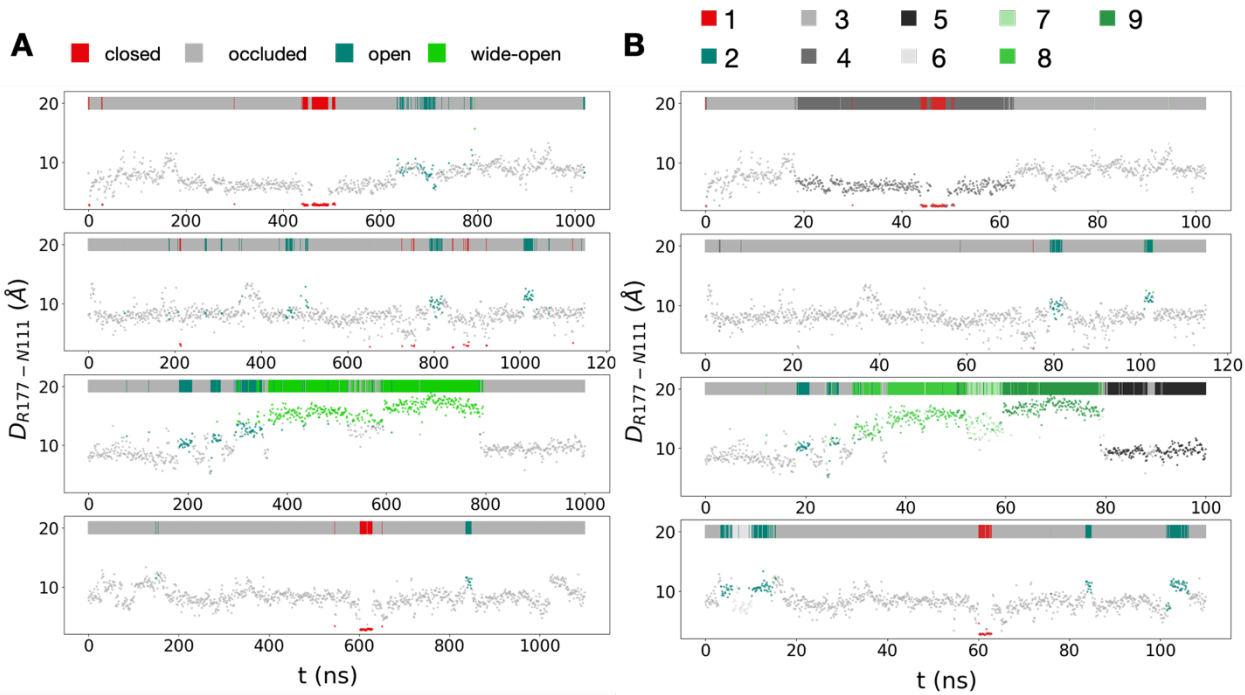

Fig. S5. Distances between R177 and N111 in four unbiased MD trajectories with states color-coded according to (A) our definitions and (B) a machine learning method called state predictive information bottleneck (SPIB) to identify metastable states automatically from the high-dimensional MD trajectories. SPIB identified substates of the occluded and wide-open states. See Table S1 for the interactions of R177 in the substates.

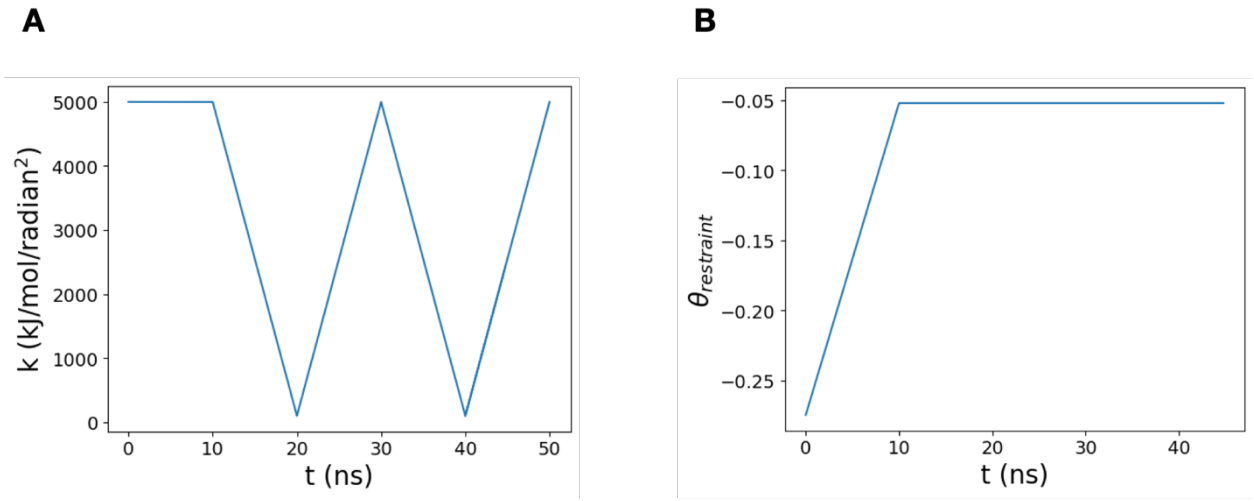

Fig. S6. (A) Variation of the force constant k and (B) the displacement of the center $\theta_{restraint}$ of the harmonic potential applied on the subunits to drive them to a flattened state. In the first 10 ns, the center of harmonic potential gradually approached the target dihedral angle (-3°) with a constant velocity and the force constant was kept at a constant of 5000 kJ/mol/radian^2. Subsequently, the center of the harmonic potential was fixed, and its force constant oscillated linearly between 5000 kJ/mol/radian^2 and 100 kJ/mol/radian^2 a period of 20 ns.

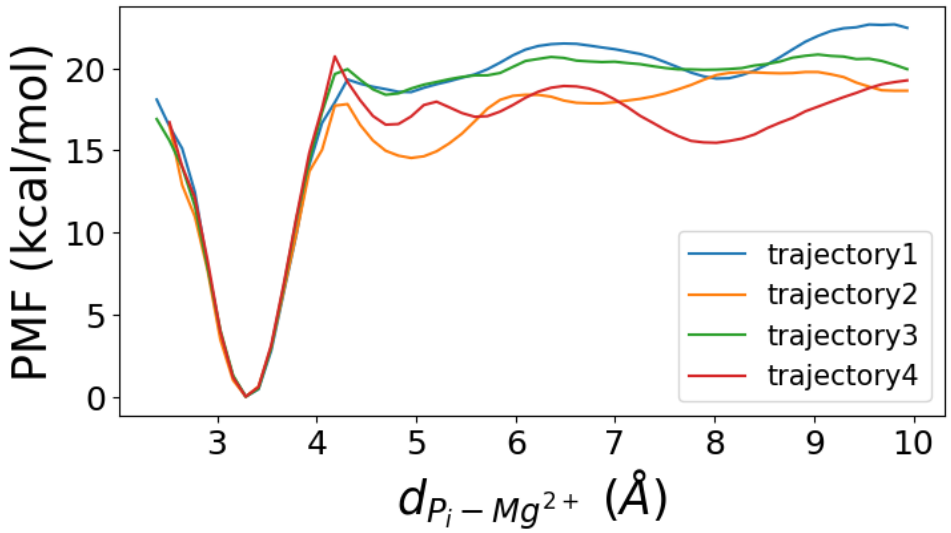

Fig. S7. The potential of mean force (PMF) profiles from four independent WT-MetaD simulations with restrained actin subunits. Harmonic restraints were added to maintain the flattened state of the terminal subunits.

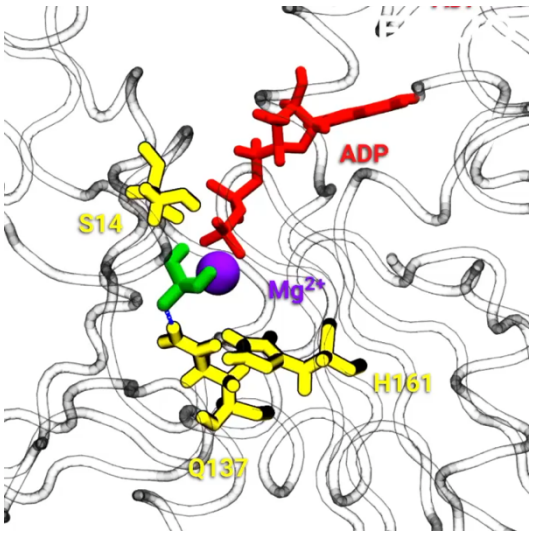

Supplementary Video 1: Time lapse video of 45 ns of time from a WT-MetaD MD simulation showing the active site of an actin filament subunit. Licorice representations show the protein backbone and stick figures show ADP (red), phosphate (green) and backbones and sidechains for residues that interact with phosphate (yellow). Mg^{2+} is shown as a purple sphere. Phosphate dissociates from Mg^{2+} only following disruption of its interaction with Q137 and reorientation of Q137 to hydrogen bond with H136.

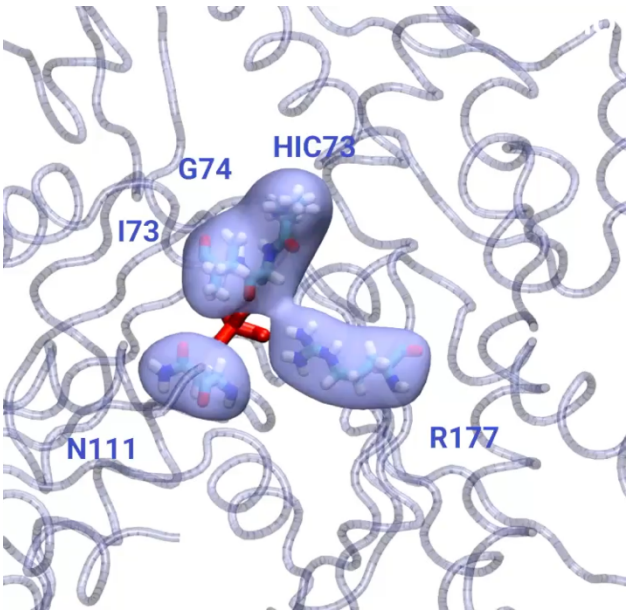

Supplementary Video 2. Time lapse video of 5 ns of time from a WT-MetaD simulation showing phosphate release from actin. Residues forming the gate are shown as stick figures inside blue surface representations. Phosphate is a red stick figure.